**ADVANCED
SCIENCE NEWS**
www.advancedsciencenews.com

**ADVANCED
MATERIALS**
www.advmat.de

COMMUNICATION

High Mobility 2D Palladium Diselenide Field-Effect Transistors with Tunable Ambipolar Characteristics

Wai Leong Chow, Peng Yu, Fucai Liu,* Jinhua Hong, Xingli Wang, Qingsheng Zeng, Chuang-Han Hsu, Chao Zhu, Jiadong Zhou, Xiaowei Wang, Juan Xia, Jiaxu Yan, Yu Chen, Di Wu, Ting Yu, Zexiang Shen, Hsin Lin, Chuanhong Jin, Beng Kang Tay,* and Zheng Liu*

Due to the intriguing optical and electronic properties, 2D materials have attracted a lot of interest for the electronic and optoelectronic applications. Identifying new promising 2D materials will be rewarding toward the development of next generation 2D electronics. Here, palladium diselenide ($PdSe_2$), a noble-transition metal dichalcogenide (TMDC), is introduced as a promising high mobility 2D material into the fast growing 2D community. Field-effect transistors (FETs) based on ultrathin $PdSe_2$ show intrinsic ambipolar characteristic. The polarity of the FET can be tuned. After vacuum annealing, the authors find $PdSe_2$ to exhibit electron-dominated transport with high mobility ($\mu_{e\,(max)} = 216$ cm^2 V^{-1} s^{-1}) and on/off ratio up to 10^3. Hole-dominated-transport $PdSe_2$ can be obtained by molecular doping using F_4-TCNQ. This pioneer work on $PdSe_2$ will spark interests in the less explored regime of noble-TMDCs.

The absence of intrinsic band gap in graphene has prompted the researchers to look for alternative 2D materials.[1] One of which is transition metal dichalcogenides (TMDCs) with the structure in the form of X–M–X, where M is a transition metal element from group 4–7 and 10, while X is a chalcogen (S, Se, Te). Although bulk crystalline TMDCs have been well-studied in the past, exploring their properties in the 2D limit has just begun. TMDC is now inviting a broad interest because of its rich chemistry and diverse properties, including insulators (HfS_2, etc.), semiconductors (MoS_2, etc.), semimetals (WTe_2, etc.), and metals (VSe_2, etc.).[2,3] Visiting this class of materials in their ultrathin form will certainly bring about significant contribution in the fast growing 2D community.

One of the most promising and well-studied TMDCs is semiconducting MoS_2. Previous studies on MoS_2 have shown its great potential in electronic,[4–7] optoelectronic,[8,9] and valleytronic applications.[10–12] The success of MoS_2 is encouraging and is the key driver toward the exploration of other promising members in the huge transition metal dichalcogenide (TMDC) family. Apart from Mo and W based 2D dichalcogenides, several new 2D members have been introduced recently. For example, the thickness independent direct band gap of ReS_2 coupled with its high external quantum efficiency makes it an attractive choice for optoelectronics.[13,14] Recently discovered narrow bandgap black phosphorus has attracted a lot of interests due to its high carrier mobility,[15] as well as the good ambipolar behavior.[16,17] Searching new narrow bandgap 2D materials with high performance as field-effect transistors (FETs) will be quite promising for future complementary logic electronics. To this end, we introduce $PdSe_2$ into the rapid growing 2D family with experimental demonstration of high mobility ultrathin channel FETs. Briefly, as-fabricated $PdSe_2$

Dr. W. L. Chow, Dr. X. Wang, Prof. B. K. Tay
Centre for Micro-/Nano-electronics (NOVITAS)
School of Electrical and Electronic Engineering
Nanyang Technological University
50 Nanyang Avenue, Singapore 639798, Singapore
E-mail: EBKTAY@ntu.edu.sg
Dr. W. L. Chow, Dr. X. Wang, Prof. Z. Shen, Prof. B. K. Tay, Prof. Z. Liu
CINTRA UMI CNRS/NTU/THALES
Singapore 637553, Singapore
E-mail: z.liu@ntu.edu.sg
Dr. P. Yu, Dr. F. Liu, Dr. Q. Zeng, C. Zhu, J. Zhou, Prof. Z. Liu
Centre for Programmed Materials
School of Materials Science and Engineering
Nanyang Technological University
50 Nanyang Avenue, Singapore 639798, Singapore
E-mail: fucailiu@gmail.com

J. Hong, X. Wang, Prof. C. H. Jin
State Key Laboratory of Silicon Materials
School of Materials Science and Engineering
Zhejiang University
Hangzhou, Zhejiang 310027, P. R. China
C.-H. Hsu, D. Wu, Prof. H. Lin
Department of Physics
National University of Singapore
Singapore 117542, Singapore

J. Xia, Dr. J. Yan, Y. Chen, Prof. T. Yu, Prof. Z. Shen
School of Physical and Mathematical Sciences
Nanyang Technological University
21 Nanyang Link, Singapore 639798, Singapore
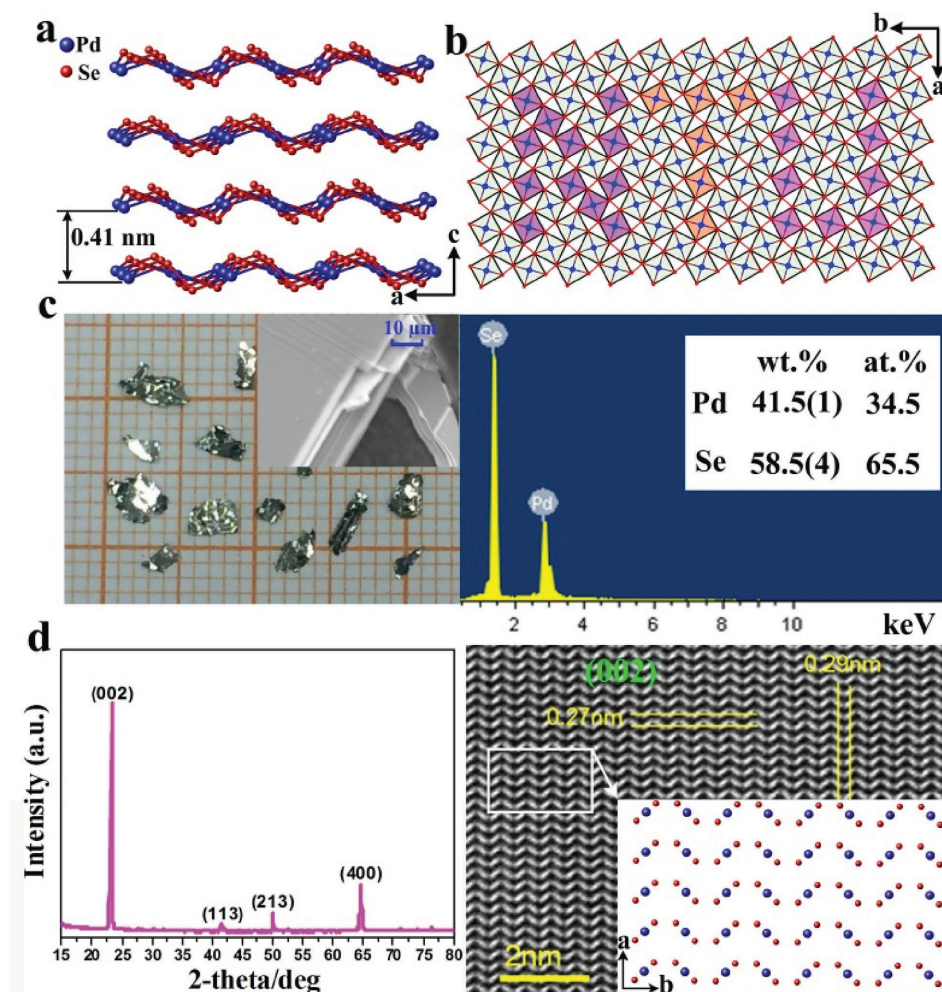
Figure 1. a) Crystal structure of PdSe$_2$ along c axis and the thickness of monolayer is 0.41 nm. b) The pucked PdSe$_2$ layer along a–b plane is composed of PdSe$_4$ tetragon, interestingly, we used the PdSe$_4$ tetragon to construct "NTU", the logo of Nanyang Technological University. c) Photographs of the as-grown PdSe$_2$ single crystals on a millimeter-grade paper (left panel) and the SEM image of the single crystal in lateral view, from which EDXS (right panel) were collected. d) The X-ray spectra (left) and the high-resolution TEM image of the (002) planes (right), which well agrees with the crystal structure of PdSe$_2$ along c axis (the inset of left panel).

FETs exhibit ambipolar characteristics and can be tuned into hole-transport-dominated (molecular doping with F$_4$-TCNQ) or electron-transport-dominated (after vacuum annealing) FETs. In particular, high mobility of ≈216 cm^2 V^{-1} s^{-1} with on/off ratio of 10^3 was realized on a 9 nm thick n-type PdSe$_2$ FET. We believe this work will lay the foundation and attract further interests in the less explored noble-TMDCs.

The layered compound PdSe$_2$ crystallizes in space group *Pbca* (No. 61) with an orthorhombic unit cell of $a = 5.7457(4)$ Å, $b = 5.8679$ (4) Å, $c = 7.6976$ (3) Å, and $V = 259.43(5)$ Å^3.[18] It has been theoretically predicated to have unique optical and thermoelectric properties.[19] Compared to the structure of traditional 1T and 2H TMDC, PdSe$_2$ has relatively waved Pd–Se layers (**Figure 1**a), which are composed of PdSe$_4$ tetragon that connects to each other to form the waved layers by Se atoms, as illustrated in Figure 1a,b. The most remarkable difference, however, is that one Pd atom is coordinated with four Se atoms, compared with six coordinated metal atoms in traditional 1T and 2H TMDC. This difference gives rise to a huge different

crystal field for Pd atoms in order to crystallize the layered structure, which possibly brings about a disparate electronic field.

The PdSe$_2$ single crystals were grown by a self-flux method, different with the one adapted in the previous report.[18] Powders of the elements Pd (99.98%) and Se (99.94%), all from Alfa Aesar, in an atomic ratio of Pd:Se = 1:6 were thoroughly mixed together, loaded, and sealed in an evacuated quartz ampule, which was slowly heated up to 850 °C, held for 50 h, Next, and then slowly cooled to 450 °C at a rate of 3 °C h^{-1}, finally to room temperature. Shiny single crystal flakes were obtained by cleaving an ingot along the layer perpendicular to the c axis, as shown in the left panel of Figure 1c. The panel in the top right corner is the scanning electron microscope (SEM) image of the layered PdSe$_2$ single crystal. The chemical composition was determined by energy dispersive X-ray spectroscopy (EDXS), which gives the atomic ratio Pd:Se pretty close to 1:2 shown in the right panel of Figure 1c. At the same time, the PdSe$_2$ phase was confirmed by the X-ray diffraction (XRD) pattern, which shows a strong gain orientation along the c axis due

**ADVANCED
SCIENCE NEWS**
www.advancedsciencenews.com

**ADVANCED
MATERIALS**
www.advmat.de

COMMUNICATION

to the layered crystal structure along the *c* axis, as displayed in the left panel of Figure 1d.

The high-resolution transmission electron microscopy (HRTEM) was explored to examine the atomic structure of $PdSe_2$, as shown in the right panel of Figure 1d. The HRTEM image of (002) plane is completely consistent with the crystal structure along the *c* axis. In addition, the electronic band structures of bulk (**Figure 2**a) and 9 nm thickness (Figure 2b) $PdSe_2$ have been obtained by the first-principles density functional theory (DFT). For bulk $PdSe_2$, the maximum of valence band is located at the Γ point, while the bottom of conduction band is not, indicating the bulk $PdSe_2$ a semiconductor with an indirect band gap. As shown in Figure 2b, the 9 nm thick $PdSe_2$ is also an indirect-band-gap semiconductor. The band gap values are found to be 0.15 and 0.16 eV for the bulk and 9 nm thick $PdSe_2$, respectively. Moreover, we also found that the band gap of the 9 nm thick $PdSe_2$ is diminished to zero when an out-of-plane electric field with strength of ± 4 mV Å^{-1} is applied. When the strength of the out-of-plane electric field is larger, a semimetallic state was obtained. This implies an electric filed controlled phase transition in $PdSe_2$ thin film.

Raman spectroscopy has become a very powerful tool for studying 2D materials like graphene and MoS_2.[20–23] The characterization on the Raman spectroscopic behavior of bulk and few layer (around 6 nm) $PdSe_2$ has been systematically

investigated using experimental and computational methods. Figure 2c displays the Raman spectra of bulk and few layered $PdSe_2$ excited by the 532 nm laser. Raman spectrum of bulk $PdSe_2$ exhibits four distinct Raman peaks at ≈143, ≈206, ≈222, and ≈256 cm^{-1} for the measurement above 100 cm^{-1}. The calculated results of bulk $PdSe_2$ (Figure 2d, Table S1, Supporting Information) show the first three modes of ≈143, ≈206, and ≈222 cm^{-1} (defined as A_g, A_g, and B_{1g}, shown in Figure 2d), can be dominated by the movements of Se atoms, while the highest mode at 256 cm^{-1} (defined as A_g, Figure 2d) involves the relative movements between Pd and Se atoms (A_g mode). Interestingly, we found that the lowest frequency at ≈143 cm^{-1} displays a broad asymmetrical peak feature due to its origin mainly from the A_g modes and a gentle mixture of B_{1g}, B_{2g}, and B_{3g} modes. The peak at ≈206 cm^{-1} can be assigned to the contributions of A_g motions and the peak at ≈222 cm^{-1} is attributed to B_{1g} modes. In addition, we noted that some new peaks are found in Raman spectra of few layer $PdSe_2$, which can be explained by the calculated results of few layer (Table S2, Supporting Information) showing that the space group will change from *Pbca* to *Pca*2_1 with $PdSe_2$ evolving from bulk to few-layer, resulting in the presence of new Raman peaks in few-layer samples, forbidden in bulk.

To investigate the transport properties of $PdSe_2$, we characterized FETs based on a back-gated configuration shown in
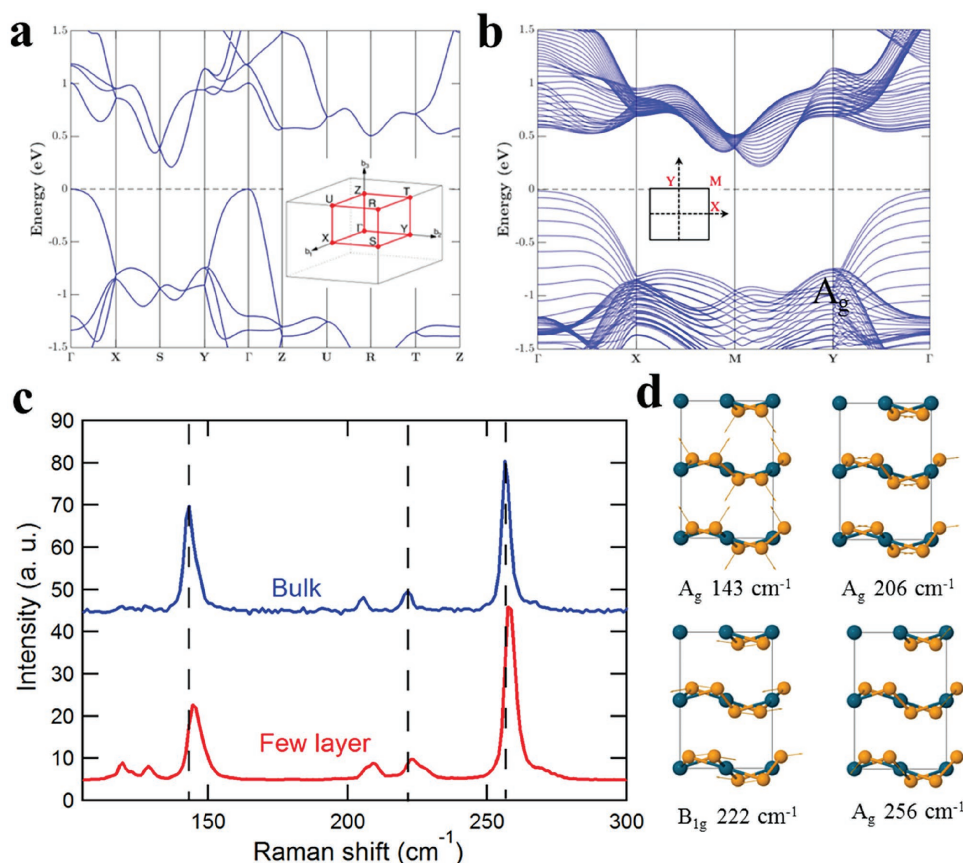
Figure 2. The calculated electronic band structures of a) bulk and b) 9 nm thick $PdSe_2$ with band gaps of 0.15 and 0.16 eV, respectively. The inset in each figure shows the Brillouin zone. c) Raman spectra of bulk and few-layer $PdSe_2$. The main peaks in the spectra for bulk structure can be assigned to d) four main Raman-active vibrational modes dominated by the movements of Se atoms. Cyan: Pd atom, yellow: Se atom.
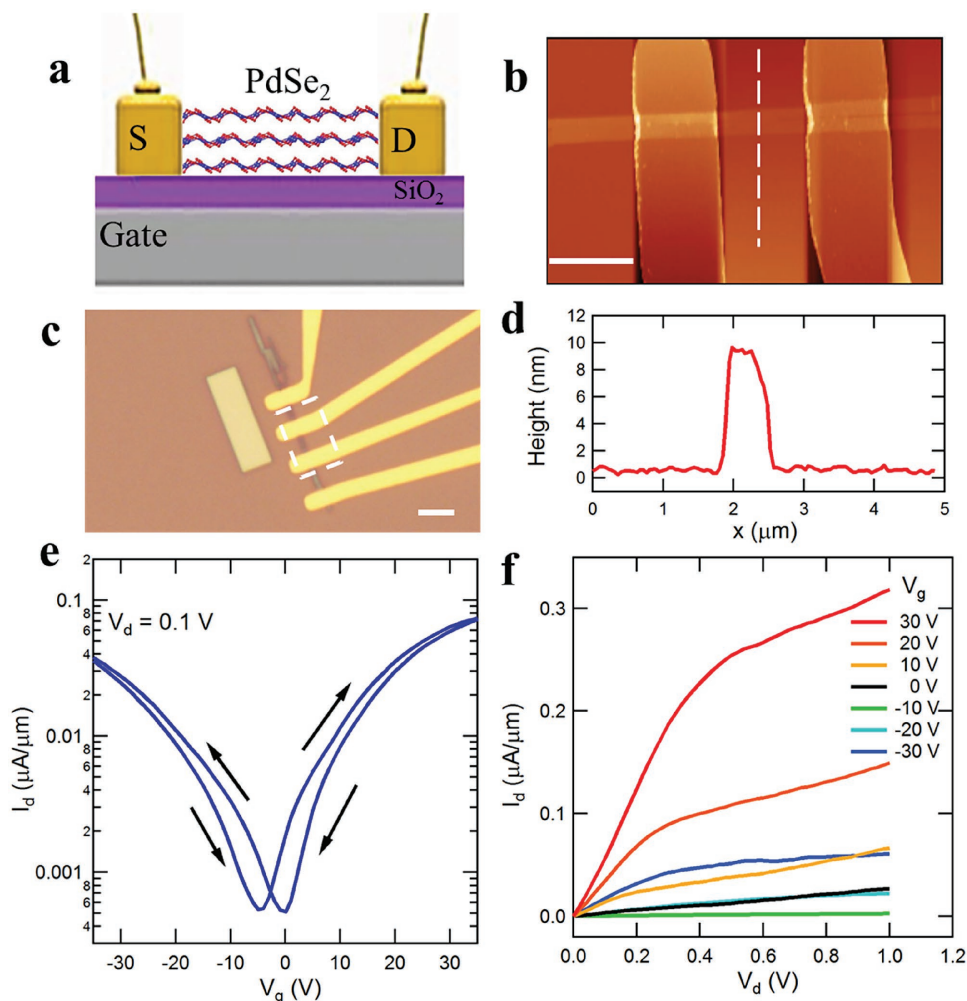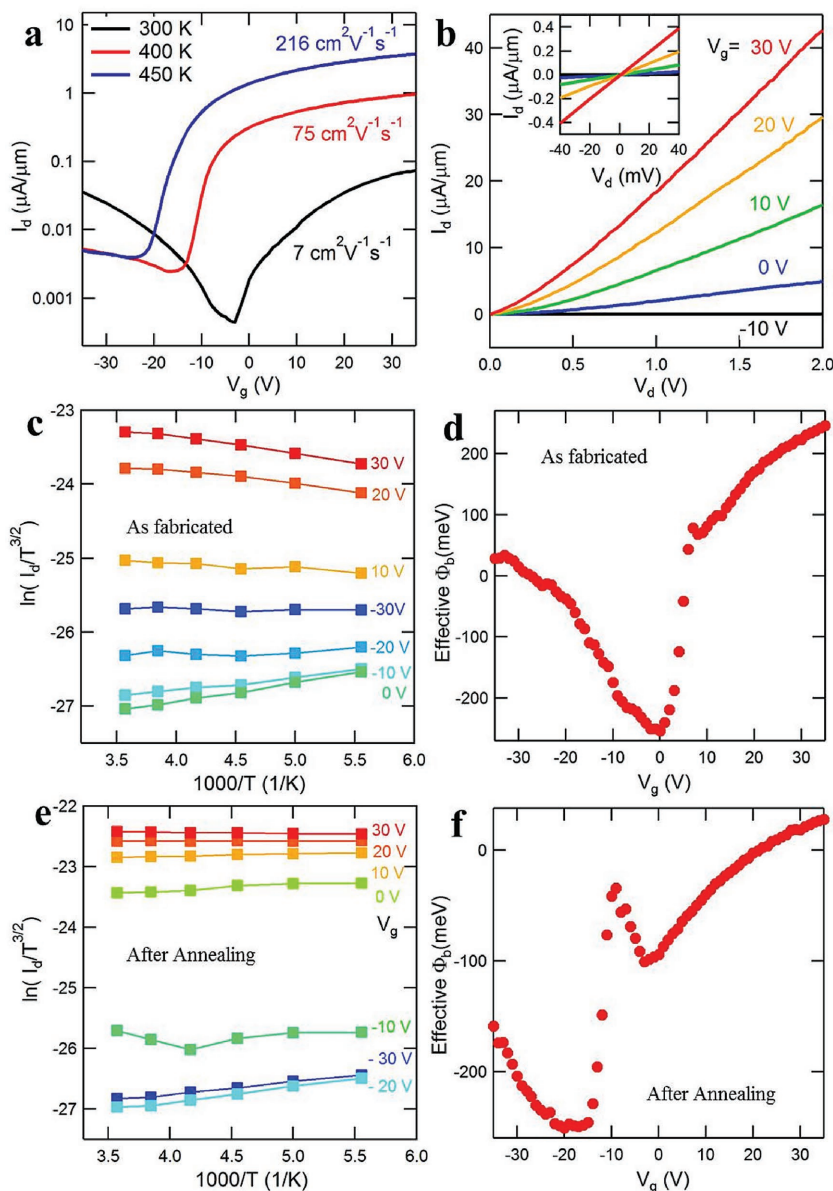
Figure 3. a) Schematic representation and b) AFM image with height profile d) of the PdSe$_2$ FET. Scale bar, 2 µm. c) Typical optical image of PdSe$_2$ devices, the area in dotted square is selected for AFM measurement. Scale bar, 5 µm. e) Transfer curve and f) output current of the PdSe$_2$ FET illustrating ambipolar carrier transport.

Figure 3a. Previous studies have shown that 2D materials with ≈10 nm have the highest mobility.[5,24] Hence, in this preliminary study, we only focus on ultrathin PdSe$_2$ with thickness between 7 and 17 nm. Figure 3c shows a typical optical image of the PdSe$_2$ device, the atomic force microscopic (AFM) image and height profile are shown in Figure 3b,d. Figure 3e,f displays the transfer curve and output characteristic of the PdSe$_2$ FET by sweeping the gate bias from −30 to +30 V. The drain current decreases first and reaches the minimum value at around zero voltage. Then it goes up with an increasing gate bias, suggesting an ambipolar carrier transport behavior. In fact, the as fabricated PdSe$_2$ FET shows a linear current drive at low drain voltage (Figure S1a, Supporting Information), indicating low Schottky barrier. The observed mild hysteresis is attributed to possible surface adsorbates from the fabrication process. The field-effect mobility was estimated from the linear region in the transfer curve by using the equation: The mobility of the carriers can be calculated by $\mu = \dfrac{L}{W \times (\varepsilon_0 \varepsilon_r / d)} \times \dfrac{dI_{ds}}{dV_G} \times \dfrac{1}{V_{ds}}$, where L, W and d denote the channel length, width, and the thickness

of SiO$_2$ layer (285 nm in our devices), ε_0 and ε_r are the vacuum dielectric constant and the dielectric constant of SiO$_2$ ($\varepsilon_r = 3.9$), respectively. For the 9 nm PdSe$_2$ shown in Figure 3e, the electron and hole mobilities are ≈7 and 5.9 cm^2 V^{-1} s^{-1} respectively, with on/off ratio of ≈10^2. More than 20 FETs were measured and their mobilities and on/off ratio are shown in Figure S1b–e in the Supporting Information. The average and maximum mobilities for these FETs are ≈($\mu_{e\,(avg)}$ = 17 cm^2 V^{-1} s^{-1}, $\mu_{h\,(avg)}$ = 7 cm^2 V^{-1} s^{-1}), and ($\mu_{e\,(max)}$ = 54 cm^2 V^{-1} s^{-1}, $\mu_{h\,(max)}$ = 14 cm^2 V^{-1} s^{-1}), respectively, with on/off ratio of up to 10^2. Such low on/off ratios are expected for PdSe$_2$ due to its small band gap[25] Also, comparing to well-explored MoS$_2$ (1–50 cm^2 V^{-1} s^{-1}), the mobility of pristine ultrathin PdSe$_2$ is commendable.

Vacuum annealing was carried out in order to improve the mobility by driving off the surface adsorbates. Measurements were conducted at room temperature after annealing the FETs for up to 450 K (system limitation). **Figure 4**a,b shows the transfer curves and output characteristic from the 9 nm PdSe$_2$ FET, respectively, where an electron-dominated carrier

**ADVANCED
SCIENCE NEWS**
www.advancedsciencenews.com

**ADVANCED
MATERIALS**
www.advmat.de

COMMUNICATION

Figure 4. a) Transfer curves of PdSe$_2$ FET showing the progressive conversion from an ambipolar transport (black curve) to a electron-transport dominated after annealing at 400 K (red curve) and 450 K (blue curve). b) Output current of a electron-transport dominated PdSe$_2$ FET obtained after annealing at 450 K. c,e) The Arrhenius plots for different back gate bias of c) as fabricated and e) after annealing PdSe$_2$ device. The slopes of the lines correspond to the Schottky barrier height for corresponding gate bias. d,f) The Schottky barrier heights for different back gate biases of d) as fabricated and f) after annealing PdSe$_2$ device, respectively.

ratio up to 10^3 was obtained after annealing at 450 K for these FETs (Figure S2b,c, Supporting Information). In particular, the 9 nm PdSe$_2$ exhibits the highest mobility of $\approx$216 cm^2 V^{-1} s^{-1} coupled with good on/off ratio of 10^3. Coincidentally, this thickness is close to the optimum thickness for high mobility MoS$_2$ and black phosphorus FETs. We believe such high electron mobility benefits from the removal of surface adsorbates. Similar effect has been observed in other 2D materials.[26–28] Annealing under vacuum would accelerate desorption of surface adsorbates, typically oxygen species which act as p-dopants, and changed the carrier doping level, similar to the observation in black phosphorus via surface charge transfer.[29] We further characterized the crystal structure before and after annealing via HRTEM, confirming that there is no change in crystal structure upon annealing (Figures S3 and S4, Supporting Information). In addition, we also fabricated one four-terminal device to evaluate the intrinsic mobility (see Figure S5 in the Supporting Information for the details). The performance of the electron-transport-dominated PdSe$_2$ FET has the potential to further improve by considering contact[5] and dielectric engineering,[4,7] making it a promising new 2D materials.

To further understand the effect of the thermal annealing, we evaluate the Schottky barrier of the device before and after vacuum annealing, via the temperature dependent measurement. As the channel is thin enough to be treated as a 2D film, the drain–source current I_d can be defined by 2D thermionic emission equation, which employs the reduced power law $T^{3/2}$ for a 2D transport channel[30–33]

$$I_d = A_{2D}^* T^{3/2} \exp\left(\frac{q\Phi_B}{k_B T}\right)\left[1 - \exp\left(\frac{qV_d}{k_B T}\right)\right] \quad (1)$$

Where A_{2D}^* is the 2D equivalent Richardson constant, T is the absolute temperature, k_B is the Boltzmann constant, q is the electronic charge, and V_d is the drain–source bias voltage. By plotting the value of $\ln(I_d/T^{3/2})$ as a function of $1000/T$ (Figure 4c,e), one can obtain the barrier height, which is the negative value of the line slope. The effective Schottky barrier as a function of gate bias is plotted in Figure 4d,f. The Schottky barrier also shows gate bias dependency. When the gate voltage sweeps from −35 to 35 V, the effective Schottky barrier first increases, and then show a dip near 0 and −10 V for the device before and after annealing, respectively, indicating the Schottky contact with opposite polarities, which is consistent with the carrier density tuning upon the gate voltage applied,[34,35] i.e., the carrier changed from hole

transport is clearly observed. From the transfer curves, one can see a progressive shift in the threshold voltage toward the negative bias (from +12.1 to −15.9 V) accompanied with an increase in drain current after annealing at 400 and 450 K, respectively. The shift in threshold voltage is an indication of the Fermi level moving toward the conduction band of PdSe$_2$. Furthermore, annealing at 450 K (Figure S2a, Supporting Information), the hysteresis in the transfer curve disappeared, implying the removal of surface adsorbates during annealing process. An average electron mobility of $\approx$ 16 cm^2 V^{-1} s^{-1}, with on/off

COMMUNICATION

dominated to neutral, and then to electron dominated when gate voltage changed from −35 to 35 V. After annealing, the Schottky barrier is largely reduced, which might be attributed to thermal annealing improved the interface contact between the metal and PdSe$_2$.[27]

Effective charge doping has been realized due to the narrow band gap and the clean surface in ultrathin PdSe$_2$. The transport nature of PdSe$_2$ can be converted into hole-transport-dominated by molecular doping using F$_4$-TCNQ as shown in **Figure 5**a,b. The structure of F$_4$-TCNQ is shown in the inset of Figure 5b, where both fluorine atoms and cyano groups are strong electron acceptors. Owing to its high electron affinity of 5.24 eV,[36] F$_4$-TCNQ is a popular choice as a p-dopant for low dimension materials, such as carbon nanotubes,[37,38] graphene[39,40] and MoS$_2$.[41] The transfer curves in Figure 5a shows the progressive conversion from an ambipolar to a hole-transport-dominated FET. Upon doping, the threshold voltage shifts toward the positive gate bias with strong suppression in the drain current. The shift in threshold voltage is due to the lowering of Fermi level when electrons from PdSe$_2$ are transferred to the F$_4$-TCNQ (Figure 5c).[38] A sight increment in

drain current is also observed and it could be attributed to the reduction in contact resistance at the metal-PdSe$_2$ interface. At the end of the fourth doping step, a hole-transport-dominated FET is achieved where the hole mobility increased from ≈7 to 12 cm^2 V^{-1} s^{-1}.

The contact resistance plays an important role on the performance of FET. To evaluate the effect of contact resistance, we carried out the transmission line measurement to qualify the contact resistances for the PdSe$_2$ devices after vacuum annealing and molecular doping. As it can be seen in Figure 5d, the contact resistance shows significant gate voltage dependence due to the Femi level tuning via electrostatic gating. The contact resistance of the as fabricated device is around 2 MΩ μm under zero gate bias, which is larger than the other 2D materials like MoS$_2$ and WSe$_2$.[42–44] The high contact resistance may be due to the mismatch between the work function of the contact metal and the PdSe$_2$ channel. Further improvement of the transistor performance could be achieved by optimizing the contact materials. The contact resistance decreased to the 0.6 MΩ μm under application of 30 V gate voltage. After thermal annealing in the vacuum, the contact
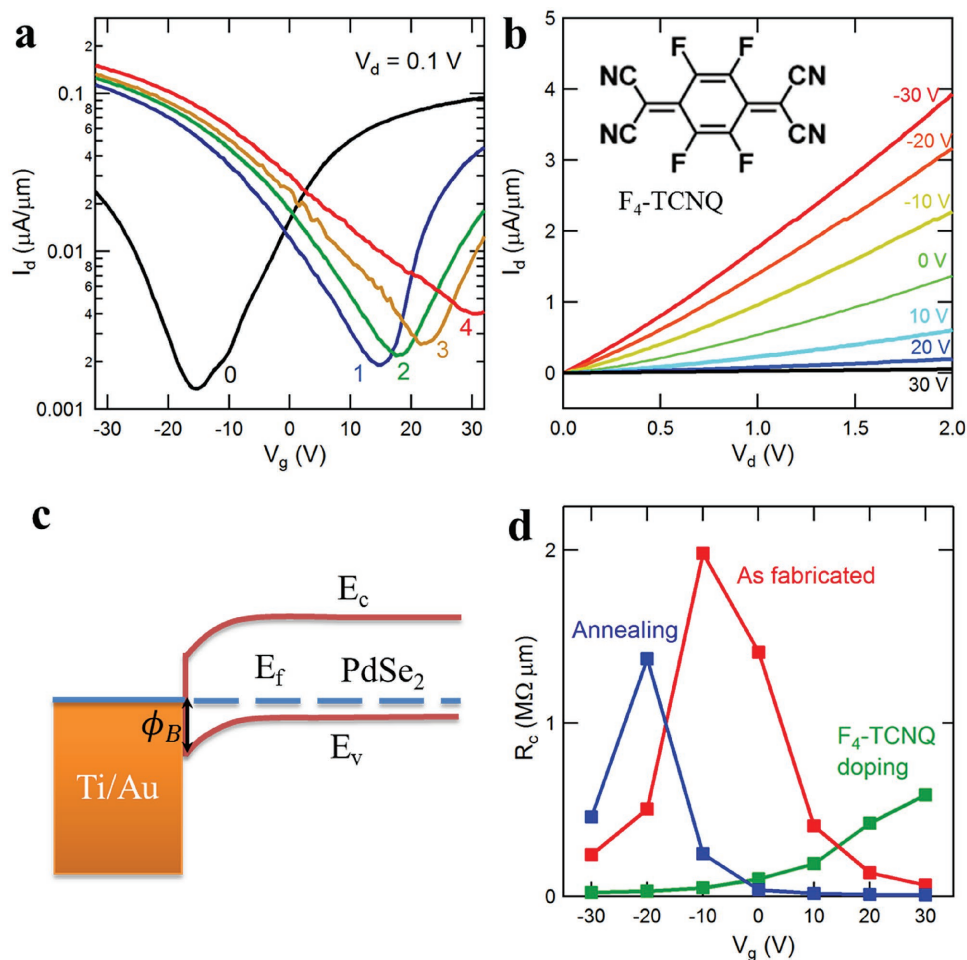
Figure 5. a) Transfer curves of PdSe$_2$ FET showing the progressive conversion from an ambipolar transport to a p-type transport. The number of doping step is indicated from 0 (undoped) to 4 (final). b) Output current of a unipolar p-type PdSe$_2$ FET obtained at the fourth doping step. The inset shows the structure of F$_4$-TCNQ. c) The band alignment at the metal-PdSe$_2$ interface after molecular doping. d) The contact resistance as a function of gate bias for as fabricated, after annealing, and molecular doping PdSe$_2$ device.

resistance reduced a lot due to the removed absorbed moisture and solvent molecules. It decreased to 0.4 MΩ μm under zero gate bias, and further decreased to 90 KΩ μm under 30 V gate bias. Molecular doping also significantly reduced the contact resistance, the contact resistance is around 100 KΩ μm at 0 V gate bias, and 22 KΩ μm obtained at −30 gate bias, around one order of magnitude smaller than the as-fabricated device, similar to the previously observation on chloride molecular doped 2D Materials.[45]

To conclude, bulk $PdSe_2$ is successfully synthesized where the crystal structure, phase, purity and composition are carefully examined by TEM, XRD, and EDS. Raman spectra of bulk and few layer $PdSe_2$ are analyzed accompanying with the theoretical calculation. As fabricated FETs based on exfoliated ultrathin $PdSe_2$ shows ambipolar transport. A simple vacuum annealing process is introduced to realize high performance unipolar n-type $PdSe_2$ FET with mobility up to ≈216 cm^2 V^{-1} s^{-1} with on/off ratio of 10^3. Lastly, $PdSe_2$ become hole-transport-dominated using molecular doping with F_4-TCNQ. The results here present $PdSe_2$ as a promising 2D materials in the fast growing 2D family and will certainly spark greater interests in the less explored regime of noble-TMDCs.

Experimental Section

Elemental Analysis: Semiquantitative microprobe analyses on the single crystals of $PdSe_2$ were performed with the aid of a field emission scanning electron microscope (JSM-5410) equipped with an EDXS (Oxford INCA). The EDS taken on visibly clean surfaces of the sample proved the presence of Pd and Se shown in Figure 1c.

Powder XRD: The powder XRD patterns were collected using a Rigaku DMAX 2500 diffractometer with monochromatized Cu-Kα radiation at room temperature in the 2θ range of 10°–85° with a scan step width of 0.05°. The measured X-ray powder diffraction patterns were in accordance with the calculated ones simulated from the single crystal data as shown in Figure 1d.

TEM Sample Preparations and ADF-STEM Imaging and Image Simulations: The TEM sample was prepared by transferring the $PdSe_2$ flakes onto lacey-carbon grid after evaporating a drop of an IPA solvent and etching away the underneath SiO_2 layer with potassium hydroxide solution. The as-prepared TEM membranes were briefly irradiated in TEM mode before annular dark-field scanning transmission electron microscopy (ADF-STEM) characterization. The ADF-STEM were done with a FEI Titan ChemiSTEM equipped with a probe corrector. This microscope was operated with an acceleration voltage of 80 kV. The convergent angle for illumination is about 22 mrad with a probe current of 70 pA, and the collection angle is about 43.4–200 mrad. ADF-STEM image simulations of pristine $PdSe_2$ were done with software STEMSIM. The input parameters were set according to the experiment conditions: collection angle is about 45–200 mrad, acceleration voltage and C3 is 80 kV and 1.5 μm respectively.

Experimental Raman Spectra of $PdSe_2$: Analysis of atomically thin $PdSe_2$ flakes and bulk sample by Raman spectroscopy was carried out on a WITec CRM200 confocal Raman microscopy system with the excitation line of 532 nm and an air-cooling charge-coupled device as the detector (WITec Instruments Corp, Germany).

The Calculations of Raman Spectra of $PdSe_2$: The crystal structure of bulk $PdSe_2$ is characterized by the space group *Pbca*, which contains 12 atoms in the orthorhombic unit cell. Among all 36 phonon modes at the Brillion zone center, 12 Raman-active modes can be expressed as $3A_g + 3B_{1g} + 3B_{2g} + 3B_{3g}$. To get estimates on the phonon frequencies, the first-principle calculations of the phonon modes at the Brillouin Zone (BZ) center were performed in the framework of the density functional perturbation theory (DFPT),[46] as implemented in CASTEP.[47] The local density approximation as parameterized by Perdew and Zunger[48] was adopted for exchange and correlation functional. A plane wave cutoff energy of 800 eV was used with a uniform 4 × 4 × 2 Monkhorst–Pack k-point mesh for integrations over the BZ. The optimized lattice parameters are a = 5.7725 Å, b = 5.8554 Å, and c = 7.384346 Å, which agree well with the experimental data (a = 5.7457 Å, b = 5.8659 Å, and c = 7.6946 Å).[49] The frequencies of the phonon modes were derived from the dynamical matrix generated by the DFPT method. The calculated frequencies and the experimental phonon modes are given in Tables S1 and S2 in the Supporting Information. With $PdSe_2$ evolving from bulk to few-layer, its space group changes from *Pbca* to *Pca*2$_1$. The irreducible representations of the optical phonons in bilayer $PdSe_2$ at the Brillion zone center (Γ point) are expressed as $8A_1 + 9A_2 + 8B_1 + 8B_2$, where all optical modes are Raman-active except there acoustic modes. This implies that some Raman peaks, forbidden in bulk, can be observed in few-layer samples, as shown in Figure 2c. Indeed, more Raman-active modes with nontrivial intensity for bilayer $PdSe_2$ present than that of bulk sample, as shown in Table S2 in the Supporting Information.

The Calculations of Band Structure of Bulk and 9 nm Thick $PdSe_2$: Full-potential first-principles calculations are based on the generalized gradient approximation within the DFT framework as implemented in the wien2k package. An 11 × 10 × 8 Monkhorst–Pack k mesh was used for the numerical integration of the Brillouin zone. To have a more accurate description for the band gap calculation, a semilocal exchange-correlation potential (mbj) was included. Wannier functions for the Se p and Pd d orbitals were constructed and a real-space tight-binding Hamiltonian was obtained. This Wannier function based tight-binding model was used to obtain the electronic structures of the 9 nm thick (24 L) $PdSe_2$.

Device Fabrication: To fabricate $PdSe_2$ FETs, thin $PdSe_2$ flakes were first exfoliated onto degenerately doped Si substrate coated with 270 nm SiO_2. Ultrathin $PdSe_2$ were identified by optical microscopy and their thicknesses were confirmed by AFM. Optical lithography was used to pattern the source and drain electrodes. Ebeam evaporator was used to deposit the metallization layer which consists of a stack of Ti (10 nm) and Au (80 nm). After evaporation, the samples were soaked in acetone overnight to lift-off the excess metal followed by cleansing with isopropyl alcohol (IPA) and deionized (DI) water.

Electrical Measurement, Vacuum Annealing, and Molecular Doping Process: Electrical measurements were carried out in a vacuum chamber (Cascade Microtech) using Keithley 4200-SCS parameter analyzer. For as-fabricated $PdSe_2$ FETs, the samples were left in the chamber overnight to achieve a vacuum condition of less than 5 × 10^{-5} mbar before measurement. For n-doped FETs, the samples were annealed up to 450 K in the vacuum chamber by resistive heating of the chunk for 2 h. This is the maximum temperature achievable by the system. Measurements were then conducted after the samples cooled down to room temperature. For p-doped FETs, a simple drop-cast method was adopted. The dopant solution was prepared by dissolving F_4-TCNQ in chloroform with a concentration of 0.02 μmol mL^{-1}. A droplet of 5 μL of the dopant solution was pipetted onto the as-fabricated FETs and left to evaporate in the vacuum chamber. Electrical measurements were carried out immediately once the vacuum reached less than 1 × 10^{-4} mbar to prevent further desorption of dopant molecules.

Supporting Information

Supporting Information is available from the Wiley Online Library or from the author.

Acknowledgements

[1] A. Gupta, T. Sakthivel, S. Seal, *Prog. Mater. Sci.* **2015**, *73*, 44.

[2] Q. H. Wang, K. Kalantar-Zadeh, A. Kis, J. N. Coleman, M. S. Strano, *Nat. Nanotechnol.* **2012**, *7*, 699.

[3] M. Chhowalla, H. S. Shin, G. Eda, L. J. Li, K. P. Loh, H. Zhang, *Nat. Chem.* **2013**, *5*, 263.

[4] B. Radisavljevic, A. Radenovic, J. Brivio, V. Giacometti, A. Kis, *Nat. Nanotechnol.* **2011**, *6*, 147.

[5] S. Das, H. Y. Chen, A. V. Penumatcha, J. Appenzeller, *Nano Lett.* **2013**, *13*, 100.

[6] H. Wang, L. L. Yu, Y. H. Lee, Y. M. Shi, A. Hsu, M. L. Chin, L. J. Li, M. Dubey, J. Kong, T. Palacios, *Nano. Lett.* **2012**, *12*, 4674.

[7] S. Kim, A. Konar, W. S. Hwang, J. H. Lee, J. Lee, J. Yang, C. Jung, H. Kim, J. B. Yoo, J. Y. Choi, Y. W. Jin, S. Y. Lee, D. Jena, W. Choi, K. Kim, *Nat. Commun.* **2012**, *3*, 1011.

[8] Z. Y. Yin, H. Li, H. Li, L. Jiang, Y. M. Shi, Y. H. Sun, G. Lu, Q. Zhang, X. D. Chen, H. Zhang, *ACS Nano* **2012**, *6*, 74.

[9] O. Lopez-Sanchez, D. Lembke, M. Kayci, A. Radenovic, A. Kis, *Nat. Nanotechnol.* **2013**, *8*, 497.

[10] K. F. Mak, K. L. He, J. Shan, T. F. Heinz, *Nat. Nanotechnol.* **2012**, *7*, 494.

[11] H. L. Zeng, J. F. Dai, W. Yao, D. Xiao, X. D. Cui, *Nat. Nanotechnol.* **2012**, *7*, 490.

[12] T. Cao, G. Wang, W. P. Han, H. Q. Ye, C. R. Zhu, J. R. Shi, Q. Niu, P. H. Tan, E. Wang, B. L. Liu, J. Feng, *Nat. Commun.* **2012**, *3*, 887.

[13] S. Tongay, H. Sahin, C. Ko, A. Luce, W. Fan, K. Liu, J. Zhou, Y. S. Huang, C. H. Ho, J. Y. Yan, D. F. Ogletree, S. Aloni, J. Ji, S. S. Li, J. B. Li, F. M. Peeters, J. Q. Wu, *Nat. Commun.* **2014**, *5*, 3252.

[14] E. Zhang, Y. B. Jin, X. Yuan, W. Y. Wang, C. Zhang, L. Tang, S. S. Liu, P. Zhou, W. D. Hu, F. X. Xiu, *Adv. Funct. Mater.* **2015**, *25*, 4076.

[15] L. Li, Y. Yu, G. J. Ye, Q. Ge, X. Ou, H. Wu, D. Feng, X. H. Chen, Y. Zhang, *Nat. Nanotechnol.* **2014**, *9*, 372.

[16] Y. Du, H. Liu, Y. Deng, P. D. Ye, *ACS Nano* **2014**, *8*, 10035.

[17] D. Yue, D. Lee, Y. D. Jang, M. S. Choi, H. J. Nam, D.-Y. Jung, W. J. Yoo, *Nanoscale* **2016**.

[18] C. Soulard, X. Rocquefelte, P. E. Petit, M. Evain, S. Jobic, J. P. Itie, P. Munsch, H. J. Koo, M. H. Whangbo, *Inorg. Chem.* **2004**, *43*, 1943.

[19] J. Sun, H. Shi, T. Siegrist, D. J. Singh, *Appl. Phys. Lett.* **2015**, *107*, 153902.

[20] M. A. Pimenta, E. del Corro, B. R. Carvalho, C. Fantini, L. M. Malard, *Acc. Chem. Res.* **2014**, *48*, 41.

[21] H. Li, Q. Zhang, C. C. R. Yap, B. K. Tay, T. H. T. Edwin, A. Olivier, D. Baillargeat, *Adv. Funct. Mater.* **2012**, *22*, 1385.

[22] L. Malard, M. Pimenta, G. Dresselhaus, M. Dresselhaus, *Phys. Rep.* **2009**, *473*, 51.

[23] A. C. Ferrari, D. M. Basko, *Nat. Nanotechnol.* **2013**, *8*, 235.

[24] L. K. Li, Y. J. Yu, G. J. Ye, Q. Q. Ge, X. D. Ou, H. Wu, D. L. Feng, X. H. Chen, Y. B. Zhang, *Nat. Nanotechnol.* **2014**, *9*, 372.

[25] F. Hulliger, *J. Phys. Chem. Solids* **1965**, *26*, 639.

[26] R. A. Doganov, S. P. Koenig, Y. Yeo, K. Watanabe, T. Taniguchi, B. Özyilmaz, *Appl. Phys. Lett.* **2015**, *106*, 083505.

[27] D. Ovchinnikov, A. Allain, Y.-S. Huang, D. Dumcenco, A. Kis, *ACS Nano* **2014**, *8*, 8174.

[28] H. Schmidt, S. Wang, L. Chu, M. Toh, R. Kumar, W. Zhao, A. Castro Neto, J. Martin, S. Adam, B. Özyilmaz, *Nano Lett.* **2014**, *14*, 1909.

[29] D. Xiang, C. Han, J. Wu, S. Zhong, Y. Liu, J. Lin, X.-A. Zhang, W. P. Hu, B. Özyilmaz, A. C. Neto, *Nat. Commun.* **2015**, *6*, 6485.

[30] J. Wang, Q. Yao, C. W. Huang, X. Zou, L. Liao, S. Chen, Z. Fan, K. Zhang, W. Wu, X. Xiao, *Adv. Mater.* **2016**, *28*, 8302.

[31] J.-R. Chen, P. M. Odenthal, A. G. Swartz, G. C. Floyd, H. Wen, K. Y. Luo, R. K. Kawakami, *Nano Lett.* **2013**, *13*, 3106.

[32] Y. Zhou, Y. Han, Y. Wang, F. Xiu, J. Zou, R. Kawakami, K. L. Wang, *Appl. Phys. Lett.* **2010**, *96*, 102103.

[33] A. Anwar, B. Nabet, J. Culp, F. Castro, *J. Appl. Phys.* **1999**, *85*, 2663.

[34] M. V. Kamalakar, B. Madhushankar, A. Dankert, S. P. Dash, *Small* **2015**, *11*, 2209.

[35] H.-M. Li, D.-Y. Lee, M. S. Choi, D. Qu, X. Liu, C.-H. Ra, W. J. Yoo, *Sci. Rep.* **2014**, *4*, 4041.

[36] W. Y. Gao, A. Kahn, *Appl. Phys. Lett.* **2003**, *82*, 4815.

[37] T. Takenobu, T. Kanbara, N. Akima, T. Takahashi, M. Shiraishi, K. Tsukagoshi, H. Kataura, Y. Aoyagi, Y. Iwasa, *Adv. Mater.* **2005**, *17*, 2430.

[38] Y. Nosho, Y. Ohno, S. Kishimoto, T. Mizutani, *Nanotechnology* **2007**, *18*, 415202.

[39] C. Coletti, C. Riedl, D. S. Lee, B. Krauss, L. Patthey, K. von Klitzing, J. H. Smet, U. Starke, *Phys. Rev. B* **2010**, *81*, 235401.

[40] W. Chen, S. Chen, D. C. Qi, X. Y. Gao, A. T. S. Wee, *J. Am. Chem. Soc.* **2007**, *129*, 10418.

[41] S. Mouri, Y. Miyauchi, K. Matsuda, *Nano Lett.* **2013**, *13*, 5944.

[42] W. Liu, J. Kang, D. Sarkar, Y. Khatami, D. Jena, K. Banerjee, *Nano Lett.* **2013**, *13*, 1983.

[43] H. Liu, M. Si, Y. Deng, A. T. Neal, Y. Du, S. Najmaei, P. M. Ajayan, J. Lou, P. D. Ye, *ACS Nano* **2013**, *8*, 1031.

[44] H. Liu, A. T. Neal, P. D. Ye, *ACS Nano* **2012**, *6*, 8563.

[45] L. Yang, K. Majumdar, H. Liu, Y. Du, H. Wu, M. Hatzistergos, P. Hung, R. Tieckelmann, W. Tsai, C. Hobbs, *Nano Lett.* **2014**, *14*, 6275.

[46] S. Baroni, S. De Gironcoli, A. Dal Corso, P. Giannozzi, *Rev. Mod. Phys.* **2001**, *73*, 515.

[47] S. J. Clark, M. D. Segall, C. J. Pickard, P. J. Hasnip, M. I. Probert, K. Refson, M. C. Payne, *Z. Kristallogr.—Cryst. Mater.* **2005**, *220*, 567.

[48] J. P. Perdew, A. Zunger, *Phys. Rev. B* **1981**, *23*, 5048.

[49] C. Soulard, X. Rocquefelte, P.-E. Petit, M. Evain, S. Jobic, J.-P. Itie, P. Munsch, H.-J. Koo, M.-H. Whangbo, *Inorg. Chem.* **2004**, *43*, 1943.